Available online at www.sciencedirect.com

jmr&t
Journal of Materials Research and Technology

journal homepage: www.elsevier.com/locate/jmrt

Original Article

Comparison of the protective efficiency of polymethacrylates with different side chain length for AA2024 alloy

Lisa Muñoz [a,*], Mamié Sancy [b,c], Carolina Guerra [d], Marcos Flores [e], Paulo Molina [a], Hugo Muñoz [a,d], Tamara Bruna [f], Camila Arcos [d], Marcela Urzúa [g], Maria V. Encinas [h], Maritza A. Páez [a,**]

[a] Departamento de Química de los Materiales, Facultad de Química y Biología, Universidad de Santiago de Chile, Av. L. B. O'Higgins 3363, Casilla 40, Correo, 33, Santiago, Chile
[b] Escuela de Construcción Civil, Facultad de Ingeniería, Pontificia Universidad Católica de Chile, Vicuña Mackenna 4860, Macul, Santiago, Chile
[c] Centro de Investigación en Nanotecnología Materiales Avanzados CIEN UC, Pontificia Universidad Católica de Chile, Vicuña Mackenna 4860, Macul, Santiago, Chile
[d] Departamento de Ingeniería Mecánica y Metalúrgica, Facultad de Ingeniería, Pontificia Universidad Católica de Chile, Vicuña Mackenna 4860, Macul, Santiago, Chile
[e] Laboratory of Surface and Nanomaterials, Physics Department, Faculty of Physics and Mathematics Science, Universidad de Chile, Beauchef 850, Santiago, 8370415, Chile
[f] Centro de Investigación Austral Biotech, Universidad Santo Tomas. Avenida Ejército 146, Santiago, 8320000, Chile
[g] Departamento de Química, Facultad de Ciencias, Universidad de Chile, Las Palmeras 3425, Ñuñoa, Santiago, 7800024, Chile
[h] Departamento de Ciencias del Ambiente, Facultad de Química y Biología, Universidad de Santiago de Chile, Av. L. B. O'Higgins 3363, Casilla 40, Correo 33, Santiago, Chile

ARTICLE INFO

Article history:
Received 18 March 2021
Accepted 12 November 2021
Available online 29 November 2021

Keywords:
Poly(methyl methacrylate)
Poly(butyl methacrylate)
Poly(hexyl methacrylate)
Corrosion
Protection
Coating

ABSTRACT

The protective properties of polymethacrylate coatings with different side chain lengths for 2024 aluminum alloys were studied, focusing on the chain length increase but also on the Ar-plasma pretreatment applied to the metal surface. The coatings were obtained by photopolymerization, obtaining reproducible molecular weight polymers during each process that were determined by high-performance liquid chromatography. AA2024 alloy were immersed into the polymethacrylate solution using methyl, butyl, and hexyl as monomers. Their roughness was then evaluated using atomic force microscopy. Surface hydrophobicity and contact angle hysteresis were analyzed in water and diiodomethane. Protective properties were evaluated by electrochemical impedance spectroscopy after 56 days of immersion in a 0.1 M Na_2SO_4. The alloy cross-sections were examined by field emission scanning electron microscopy and glow discharge optical emission spectroscopy, allowing the estimation of film thickness. Surface analysis revealed that the defect population densities in the coatings increased the monomer alkyl chain length. The immersion

* Corresponding author.
** Corresponding author.
E-mail addresses: lisa.munozm@usach.cl (L. Muñoz), maritza.paez@usach.cl (M.A. Páez).
https://doi.org/10.1016/j.jmrt.2021.11.067

thickness increase was consistent with contact angle measurements taken over time, and independent from the chain length. Contradicting expectations, the results showed the protective efficacy was not related to the chain length, since after exposure, the PBMA film revealed the best anti-corrosive coating performance on the AA2024. This was possibly influenced by its polymeric film conformation, hydrophilicity, ordering and lower density of defects on the metal surface.

1. Introduction

Aluminum 2024 (AA2024) is a light alloy widely used in aircraft and aerospace industries, principally due to its excellent light weight and mechanical resistance. Mechanical properties are improved significantly when alloying elements are added due to new phases being formed, while, however, the corrosion resistance decreases [1–4]. During the last 20 years, both chromic acid chromatizion and anodizing have been used commonly when treating surfaces prior to paint application in order to improve the corrosion resistance of aluminum alloys, but the presence of Cr (VI) in its residues, and the carcinogenic effect of this species, has motivated the development of other anticorrosive protocols [4,5]. Thus, the potential use of polymeric coatings with a low environmental impact that provides corrosion protection is being studied, trying to emulate the excellent protection achieved with chromate based systems [6–8]. Indeed, polymeric systems based on polymethacrylates and polyacrylates are of great interest since their properties allow them to act as promising organic materials for anticorrosive coating applications. Perrin et al. [9] studied copolymers based in butyl methacrylate/methyl methacrylate/methyl methacrylate, by increasing the content of butyl methacrylate in the coatings, as based on studies previously reported by W. Funke [10]. Funke found that these materials demonstrated good flexibility and hydrophobicity, as well as remarkable resistance to stress. Additionally, the author [10] reported that the permeability to electrolytes decreased with the rise of butyl content, improving their barrier properties. On the other hand, Ranjithkumar et al. [11] synthesized copolymers of p-acetamidophenyl methacrylate (PAPM) with N-vinyl pyrrolidone (NVP), studying their capacity as antibacterial coatings with anti-corrosion properties. The results showed good antibacterial capacity and protection against corrosión of species in a saline environment. The effectiveness of the protective ability of the polymeric system was dependent on the PAPM and NVP composition. The results suggested that functionalized methacrylate-based copolymers could be used as anticorrosive coatings. Consequently, the incorporation of methacrylate polymers with alkyl groups onto metal surfaces make it possible to obtain materials with good thermal, mechanical, chemical and stability properties, allowing them to be favorable candidates for anticorrosive applications. Additionally, acrylic resins have been shown to have several advantages as coatings, such as having excellent weather resistance, high resistance to alkaline and acid hydrolysis, and being resistant to discoloration when heating and oxidizing environments [9]. An example is the use of N-(acryloyloxymethyl) benzotriazole (AMBT) and methyl methacrylate (MMA) polymers as a protective film for mild steel samples in HCl solution [11]. Additionally, the use of poly (butyl methacrylate) (PBMA) coatings for the protection of an AZ31 alloy, submerged in a 3.5% NaCl solution, has been reported [12], where the authors estimated a lower current density for the coated alloy in comparison to the bare alloy by polarization curves, and a larger charge-transfer resistance (R_{ct}) for the coated alloy by electrochemical impedance spectroscopy (EIS), confirming its corrosion protection performance. On the other hand, changes in the dielectric constant of certain organic coatings of water-based paints in contact with 0.5 M NaCl solution have been reported [13]. In this context, water uptake has been an interesting subject in investigations related to corrosion and protection [14–18].

Changes in the hydrophobicity of the films could prevent electrolytes migrating to the metal-coating interface, which would delay the corrosion process of the metallic substrates, since the difference in polarities between the corrosive medium and coating would prevent the electrolyte penetrating the protective film. Therefore, the wettability and proper adhesion on the base material are essential in improving the efficiency of the coatings [9,19]. Recently, it has been proposed that polymer adhesion to metal can be substantially improved by a plasma pre-treatment. A study associated with poly methyl methacrylate, obtained by radical polymerization, as a coating for AA2024 included the effect of an Ar-plasma pre-treatment [20]. The hydrophilicity of the aluminum alloys increased and therefore improving the interaction of the coating with the alloy and improving its protective capacity. The strong interaction between the hydroxyl groups, generated on the surface immediately after the plasma treatment, and the functional polar groups of the monomers carrying a double bond, promotes good metal-coating adhesion [20].

As mentioned, the objective of this work was to evaluate the anticorrosive capacity of polymeric coatings based on polymethacrylates for the protection of the AA2024 alloy, studying, in particular, the influence that the length of the alkyl side chain of the monomers has on the protective characteristics of polymeric films obtained by photopolymerization of the monomers. There are few reports in the literature that correlate molecular structure with anticorrosive capabilities in applications with polymeric films derived from alkyl-methacrylates [8,12,20]. Moreover, parts of these works have been reported by our research group [8,20]. Regarding the experimental work, the degree of coating wettability was determined by contact angle hysteresis measurements. The surface morphology was examined by atomic force microscopy (AFM) and emission scanning electron

microscopy (FE-SEM) of the surfaces and the metal-coating cross-sections. Through these last observations, the thickness of the coatings was determined. The chemical composition was obtained by glow discharge optical emission spectroscopy (GD-OES). The performance of the coatings was evaluated by electrochemical techniques, such as measurements of open circuit potential and electrochemical impedance spectroscopy (EIS), after different exposure times (1–56 days) to the electrolyte.

2. Experimental

2.1. Polymerization of alkyl methacrylate monomers

Polymerizations of methacrylate monomers, namely: methyl, buthyl and hexyl methacrylate (MERCK, 99%) were carried out in tetrahydrofuran (THF) at 25 °C under a nitrogen atmosphere and started with Azobisisobutyronitrile (AIBN) (Sigma Aldrich 98%). The steady-state irradiation was performed in a Rayonet reactor with 366 nm RPR lamps. The polymers were precipitated in methanol, dissolved in THF, and subsequently applied onto the surface of AA2024 samples by immersion, as described in section 2.3. Molecular weights (Mw) were determined by SEC in THF, using a Hewlett Packard Series 1100 high-performance liquid chromatography (HPLC) with a refractive index as a detector, using a TSK-GEL column (7.5 mm × 300 mm). The Mw values were around 60.000 g mol^{-1}.

2.2. Metal sample preparation

The AA2024 aluminum alloy sheets were provided by the Compañía Aeronáutica Nacional de Chile (ENAER). The chemical analysis in% by weight was: 4.90 Cu, 1.52 Mg, 0.169 Fe, 0.52 Mn, 0.08 Si, and Al to balance. The dimensions of the specimens were 100 × 100 × 1.8 mm plates. Before coating application, these samples were polished with silicon carbide paper (grade # 400 to # 4000), degreased with methanol/water for 3 min, washed with double distilled water, and then dried under cold airflow. After mechanical polishing, the samples were treated with a 0.01 M NaOH solution for 2 min, rinsed with double distilled water and immersed in a 20% v/v HNO_3 solution for 2 min, later rinsed in double distilled water and ethanol, and finally, dried for 30 min at room temperature. In the final stage of the surface cleaning treatment, the samples were treated with a flow of Ar plasma generated by the RF power supply (13.56 MHz) inside a dielectric quartz tube placed inside a hollow electrode. The flow of the working gas exiting the nozzle formed the pure argon (Ar) plasma jet at 5 L min^{-1}. The power applied to the electrode was set at 80 W; the treatment time was 120 s at pressure of 170 torr.

2.3. Coating deposition

The samples were immersed in a 1.12 molal polymer solution for 6 min, and after withdrawing from the reactor, they were dried under a flow of cold air [20]. Table 1 provides the terminology used for labeling the samples.

2.4. Surface characterization

The cross-sections of coated AA2024 samples were examined by FE-SEM model QUANTA FEG 250 at an acceleration voltage of 10 kV. The analyses were performed on different regions of the coated samples, both before and after exposure to a 0.1 M Na_2SO_4 solution, facilitating the estimation of the coating thickness in all the samples. The chemical compositions of the samples were analyzed in depth before being exposure by using a GD-OES model Spectruma Analytik GmbH GDA 750 HR, with a 2.5 mm diameter anode operating in DC excitation mode. The analysis was carried out in an Ar atmosphere (quality 5.0) with an average discharge pressure of $5 \cdot 10^{-2}$ hPa, using the following excitation parameters: 1000 V, 12 mA, and 0.1 m min^{-1} cathodic spray rate [21]. The quantified profiles of percentage mass concentration versus depth were obtained using the standard WinGDOES software. All samples were measured in triplicate. Furthermore, AFM was used to study the surface morphology of the samples through the contact mode. The AFM equipment consisted of an Omicron SPM1 operating in an ultra-high vacuum, AFM tips of 10 nm radius, and with an elastic constant of 0.02–0.77 N m^{-1}.

Regarding the surface physicochemical properties, measurements were made for the contact angle of the samples at 25 °C, using the sessile drop method, or static drop, using a contact angle device (Drop Shape Analyzer DSA25S, KRUSS) controlled by the software ADVANCE (KRUSS). The procedure was as follows; 8 μL of drops of water or diiodomethane were deposited on the surface under study, using sessile water drops of 4 μL and 8 μL respectively for advanced contact angles (θa) and backward contact (θr), thus obtaining hysteresis in the contact angle, which is the difference between the forward angle and the retreat angle ($\Delta\theta = \theta a - \theta r$).

2.5. Electrochemical measurements

The electrochemical responses for the uncoated and coated samples under study were carried out during 56 days of exposure in a 0.1 M Na_2SO_4 solution (reagent grade). Notice that the solution allowed to better visualize the protective coating efficacy for AA2024 alloy, without hindering a localized corrosion, as previously described by Heine et al. [22,23]. In addition, a potentiostat/galvanostat (Bio-Logic, VSP) and a three-electrode cell were used. The working electrode was, according to the particular experiment, the AA2024 alloy with and without coating. The reference and counter electrodes were, mercury/mercuric sulfate (Hg/Hg_2SO_4, SSE) and a graphite rod respectively. The open-circuit potential (OCP) was recorded until reaching a steady-state, and the impedance data was recorded at the open circuit potential within

Table 1 – Sample nomenclature.

Sample	ID
AA2024 treated with mechanical polishing and chemical etching	AA
AA2024-Poly(methyl methacrylate)	AA-PMMA
AA2024-Poly(butyl methacrylate)	AA-PBMA
AA2024-Poly(hexyl methacrylate)	AA-PHMA

the frequency range of 20 kHz to 3 mHz, using a sinusoidal amplitude of 20 mV peak-to-peak, with eight points per decade.

3. Results and discussion

3.1. *Surface characterization*

Figure 1 shows AFM images of AA2024 specimen surfaces coated with the different polymers. The images reveal areas of different contrast which appear as "defects" in the polymeric film. A line profile through the flat areas gives us height value differences close to 1.3–1.5 nm for AA-PMMA and AA-PBMA, increasing to almost double, about 3.0 nm, for AA-PHMA (see Fig. S1). From surface topography images, the population densities of defects in the coatings were also estimated, obtaining the following results: AA-PMMA, 2 μm^{-2}; AA-PBMA, 6 μm^{-2}; and AA-PHMA 9 μm^{-2}. It should be noted that the higher population density of "defects" in the AA-PHMA may be related to its high surface charge. Furthermore, from the line profile inserted in Fig. 1 (a-c), the concavities show different depths; the smallest showing a size of 40–60 nm, while the largest, a size of 130–190 nm.

SEM images show the topographic difference of the samples with and without coating, as shown in Fig. 2S (a-d) in the supplementary material, where the roughness of the samples with the different coatings is revealed, as can be seen in Fig. 2S (b-d).

Figure 2(a) shows the images associated with the contact angle measurements for the samples, revealing that the contact angle values varied between 79.30° (±0.11°) and 99.8° (±0.13°) for AA-PMMA, AA-PBMA, and AA-PHMA samples, which indicate that the wettability of the polymer decreased with the length of the monomer chain. Nevertheless, said contact angle measurements should be prudently taken, considering that the roughness and porosity of the surface influence its wettability [24]. With rough surfaces, the existence of the so-called Wenzel state has been proposed, in which the surface under the liquid is drenched, incrementing the contact surface area between solid and liquid, resulting in the apparent contact angle increasing for hydrophobic surfaces and decreasing for hydrophilic surfaces [25].

It is also possible that air bubbles had become trapped between the liquid droplets and the solid surface, generating a state called Cassie-Baxter. As described in the Cassie Baxter state [26], the more heterogeneous and porous surfaces present a greater contact angle due to the previously mentioned air bubbles [27]. The presence of the air-bubbles at the surface–liquid interface could explain the greater contact angle for the AA-PHMA sample, which according to the AFM analysis, presented the highest population density of defect per micrometer square, and the lowest contact angle being estimated for the AA-PMMA sample presenting the lowest

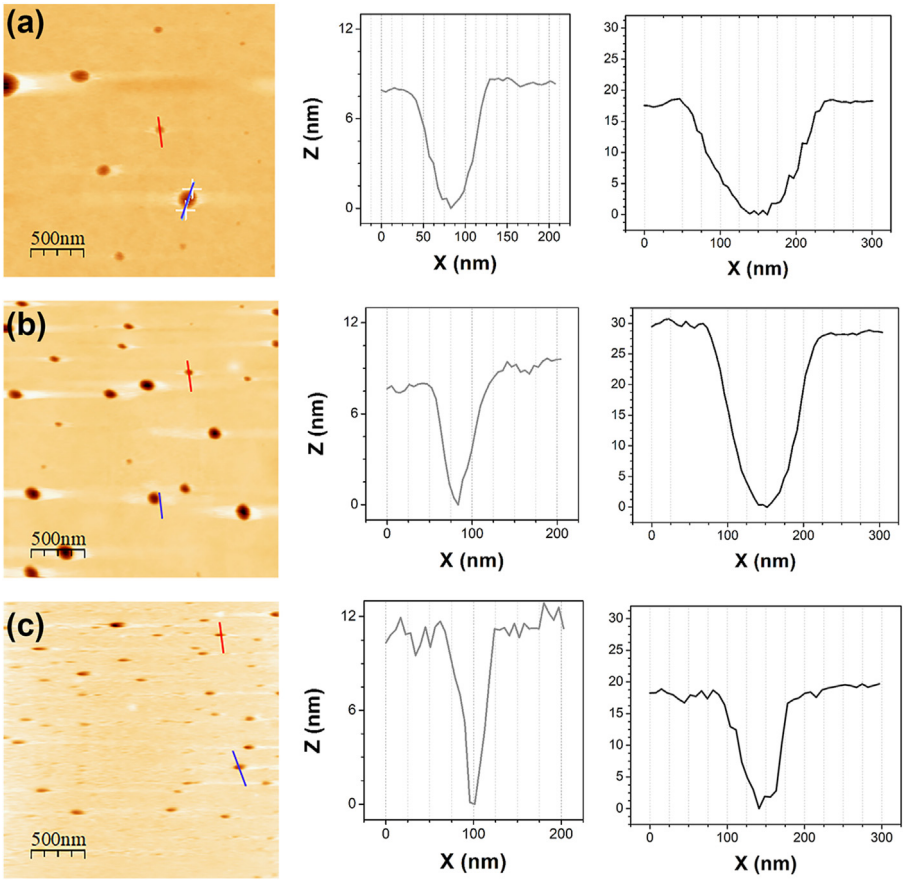

Fig. 1 – Images AFM of samples prior to exposure. (a) AA-PMMA, (b) AA-PBMA, (c) AA-PHMA.

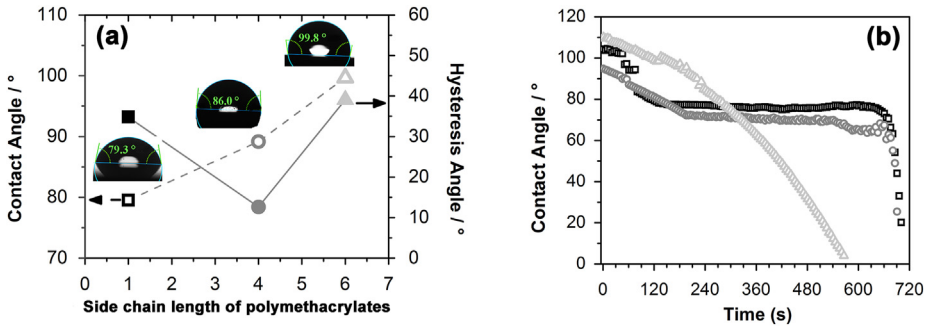

Fig. 2 – (a) Comparison of the contact angle and hysteresis angle of polymethacrylates (b) evaluation of the contact angle as a function of the immersion time of exposure of the drop (□,■) AA-PMMA (○;●) AA-PBMA and (Δ;▲) AA-PHMA.

defect population density. It seems then that the wettability of the coating surface not only depends on the length of the alkyl side chain present in each polymer, but also on the surface irregularities they present.

Figure 2(a) also reveals relatively high values of the hysteresis angle for the AA-PMMA 35.0° ± 0.17° and AA-PHMA 39.0° ± 0.12°, which is associated with the surface roughness, or surface chemical heterogeneity, suggesting that the polymers could be formed by two functional groups, hydrophobic and hydrophilic functional groups [28,29]. The AA-PBMA sample shows the lowest hysteresis angle of the three polymers studied, 12.7° ± 0.13°, which could be associated with a more homogeneous coating distribution on the metal surface that also agrees with the low roughness presented by AFM (Fig. 1S (b)). On the other hand, the surface energy was calculated by measuring the contact angle of diiodomethane and water, obtaining the following results: AA-PMMA 53.73 mN m^{-1}, AA-PBMA 42.02 mN m^{-1}, AA-PHMA 33.42 mN m^{-1}. Those values are consistent with the evaluation of the contact angles over time. Therefore the material surface energy possibly could have been influenced by factors such as the variation in the length of the monomer chain [30]. Fig. 2(b) shows the changes in the contact angle, revealing that the AA-PMMA and AA-PBMA polymers have similar stability, unlike the case of AA-PHMA, where the contact angle drop is abrupt, showing a rapid deterioration of their wettability properties.

From GD-OES analysis, the chemical composition relative to different depths for all coated samples were obtained, as shown in Fig. S3 of the supplementary material, which confirmed the homogeneity of the coatings. As can be observed, the AA-PMMA sample was composed of 87 wt.% of carbon and 11.7 wt.% of oxygen in the first 0.5 μm, which decreased significantly to 1.0 μm, 18 wt.% for carbon, and 4 wt.% for oxygen. A gradual increase in aluminum content was observed in parallel, from 0 wt.% at 0.5 μm to 53.9 wt.% at 1.0 μm (see Fig. S3 (a)). For the AA-PBMA sample, carbon and oxygen were detected between 0 μm and 6 μm, as well as the presence of carbon decreasing dramatically between 3 μm and 5.2 μm, while the oxygen content decreased from 11 wt.% to 0.7 wt.% in the same depth range. On the other hand, the aluminum content increased to 55 wt.%. At a deeper depth, aluminum and alloying elements were detected at 5.2 μm (see Fig. S3 (b)). For the AA-PHMA sample, carbon and oxygen signals were detected within the first 4.3 μm; however, the aluminum percentage gradually increased to 54 wt.% between 3 μm and 6 μm (see Fig. S3 (c)). From the GD-OES profiles, the thickness of the coatings was estimated, based on the point when the aluminum signal was constant, which was close to 1.0 μm, 5.1 μm, and 5.9 μm for AA-PMMA, AA-PBMA and AA-PHMA before exposure. It should be noticed that the accuracy of the measurements could have been strongly influenced by the coating homogeneity and surface roughness, which rose due to the Ar-pretreatment being carried out prior, but also due to the reference standards used for GD-OES analysis of the coated samples [31]. Therefore, these results are considered semi-quantitative, thus, the composition of the coatings and the Al_2O_3 layers are not stoichiometric [32]. The coating thickness for the methacrylate derivatives that were estimated by using GD-OES and SEM analysis before and after being exposed to the electrolyte are summarized in the Table 2.

On the other hand, the coating thickness for coated samples, AA-PMMA, AA-PBMA, and AA-PHMA, was also estimated from FE-SEM images, as shown in Fig. 3. Before exposure, all coated samples revealed a coating thickness between 3.1 $<\delta<$ 6.2 μm, as well as having homogeneous surfaces. The thinnest thickness was that of the AA-PMMA sample (see Fig. 3 (a)), while the thickest was that of the AA-PBMA sample (see Fig. 3 (b)). Notice that the differences in the thickness that were estimated by using GD-OES and FE-SEM analyses can be attributed to the accuracy of the techniques, but also due to the FE-SEM analysis being performed in a local area, which could also have been strongly influenced by the coating homogeneity. After 56 days of exposure, almost all coatings

Table 2 – Variation of the thicknesses of methacrylate derivatives coatings on the metal surface before and after exposure.

Coating	PMMA		PBMA		PHMA	
Exposure condition	Before	After	Before	After	Before	After
Thickness (nm) by GD-OES	1.0	n.m	5.1	n.m	5.9	n.m
Thickness (nm) by FE-SEM	3.4 ± 0.2	8.3 ± 0.6	6.2 ± 0.0	16.8 ± 1,4	5.2 ± 0.3	38.7 ± 0.7

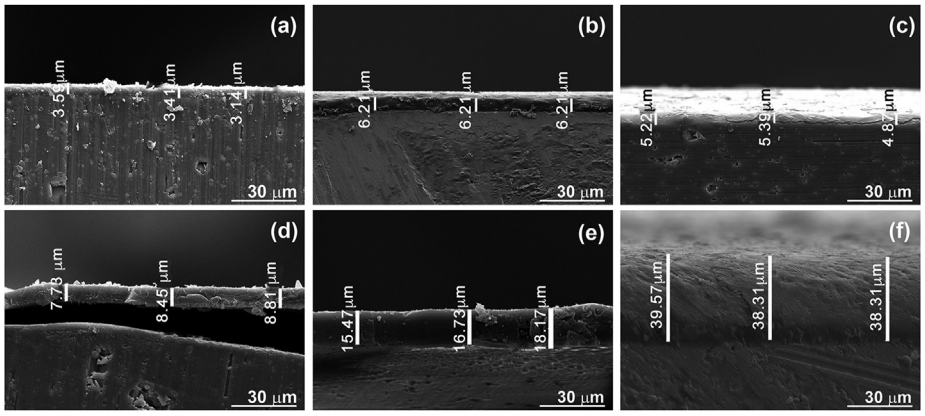

Fig. 3 – FE-SEM cross-section images of coated samples (a,b,c) prior to and (d,e,f) after a 56 days exposure in 0.1 M Na_2SO_4 solution (a,d) AA-PMMA (b,e) AA-PBMA and (c,f) AA-PHMA samples.

showed an increase in thickness. In particular, the AA-PMMA film revealed an increase in thickness and a loss of adhesion to the surface (see Fig. 3 (d)). This could be related to water absorption, according to the contact angle behavior over time, as shown in Fig. 2 (b), as reported by different authors in literature [13,16,33]. Furthermore, it also appears that the AA-PBMA film is the one with the lowest increase in thickness after exposure (Fig. 3 (e)).

3.2. *Electrochemical behavior*

Figure 4 shows the Nyquist plot for AA-PMMA, AA-PBMA, and AA-PHMA after 1 and 56 days of exposure to 0.1 M of Na_2SO_4, and the equivalent circuit proposed. All samples exhibited two capacitive loops, a sigle time constant at high range (HF) and another at low-frequency range (LF). As can be also seen in Bode plots, as shown in Fig. S4. The capacitance (C) of each time constant was estimated through equation (1) at its characteristic frequency (f_c) [34]:

$$C = \frac{1}{(2\pi f_c) \times 2r} \quad (1)$$

where 2r represents the diameter of the capacitive loop. C values varied from 9.5 × 10^{-4} to 1.71 × 10^{-3} µF cm^{-2} at HF range, while C was larger at LF range, varying from 0.1 to 1.7 µF cm^{-2}. The total impedance for all the coated samples decreased after 56 days, suggesting that the protective coating properties decrease considerably over time, leaving the metal surface exposed. However, this reduction was less dramatic for the AA-PBMA sample in respect to AA-PMMA and AA-PHMA. The time-constants at HF and LF domains were assigned to the coating and the electric double layer (C_{dl}) due to the capacitance values, respectively, as has been priorly reported [35–37]. It is worth mentioning that for the uncoated sample (AA), Nyquist and Bode plots revealed a capacitive response with a single time-constant associated with the alumina oxide formation, as reported by Blanc et al. [3], Nguyen et al. [13], and Muñoz et at. [20], which can also be observed in Figs. S5 and S6 in the supplementary material.

All coated samples showed non-ideal capacitive behavior at whole frequencies due to their current and potential distribution over the surface [38], revealing a constant phase element (CPE) behavior that can be represented by the CPE parameters, Q and α. Fig. 4(c) shows the proposed equivalent circuit, where CPE_C and CPE_{dl} correspond to the coating and the electric double layer capacitances. Additionally, the R_e represents the electrolyte resistance, while the R_C corresponds to the coating resistance, and the R_{ct} represents the charge transfer-resistant that occurs in the coating/metal interface. Table 3 summarizes the fitting parameters.

Table 3 shows that for AA-PMMA and AA-PHMA samples, Q_C values increased and $-\alpha_C$ decreased over time. While for the AA-PBMA sample, both CPE parameters varied slightly during exposure. In particular, for AA-PBMA the $-\alpha_C$ values were close

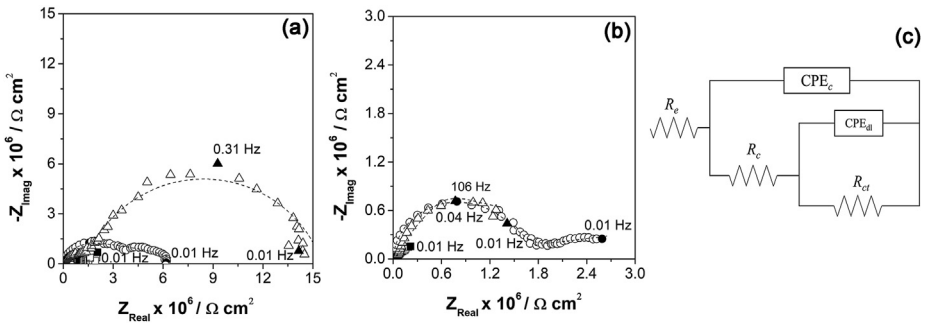

Fig. 4 – Nyquist diagrams of coated AA-2024 after (a) 1 day, (b) 56 day of exposure in 0.1 M Na_2SO_4 solution at E = OCP, and (c) equivalent circuit (---) Fit and experimental data obtained for (□) AA-PMMA (○) AA-PBMA, and (Δ) AA-PHMA.

Table 3 – EIS Fitting parameters.

ID	t (days)	CPE_c		CPE_{dl}		R_c x10^4 (Ω cm^2)	R_{ct} x10^5 (Ω cm^2)
		$-\alpha_C$ (–)	$Q_C \times 10^{-9}$ ($F \cdot s^{(\alpha-1)} \cdot cm^{-2}$)	$-\alpha_{dl}$ (–)	$Q_{dl} \times 10^{-9}$ ($F \cdot s^{(\alpha-1)} \cdot cm^{-2}$)		
AA-PMMA	1	0.89	1.96	0.45	1.01	91.7	11.7
	7	0.57	300.00	0.59	13.00	1.5	2.9
	28	0.48	915.00	0.47	19.40	1.3	6.2
	56	0.64	244.00	0.55	26.40	1.1	8.2
AA-PBMA	1	0.98	0.72	–	–	106.0	–
	7	0.95	1.10	–	–	210.0	–
	28	0.97	0.93	–	–	89.0	–
	56	0.96	1.10	–	–	100.0	–
AA-PHMA	1	0.80	2.50	0.80	0.03	151.0	140.0
	7	0.79	8.15	0.77	0.07	48.0	140.0
	28	0.69	67.60	0.67	0.37	2.8	93.5
	56	0.61	173.00	0.70	2.30	2.2	46.0

to −1, which were higher than the $-\alpha_C$ values for AA-PMMA and AA-PHMA, possibly due to AA-PBMA was more homogenious, suggesting also the best protective capabilities. Moreover, it should be noticed that the CPE parameters associated with the electric double layer were revealed for AA-PMMA and AA-PHMA samples, which increased during exposure. In this context, Boucher et al. [37], proposed that the low Q_{dl} values can be associated with the low metal surface area exposed to the electrolyte.

Figure 5 shows the Bode plot for AA-PMMA, AA-PBMA, and AA-PHMA samples after 56 days of exposure. As mentioned above, the coated samples exhibited two constants of time, typical of coating/metal systems [15,39,40]. However, it should be also noticed that the second loop at LF appeared for a longer exposure time, which can be associated with the double layer response of the metal, suggesting a breakdown of the coating. Fig. 5(a) reveals that AA-PBMA had the highest modulus when compared to the other samples. Therefore, it seems that the length of the aliphatic chain does not have a relation with the coating anticorrosive capability [41]. This agrees with the angle analysis, where for instance, the angle dropped abruptly for AA-PHMA, suggesting a quick water uptake that deteriorates their protection properties.

CPE parameters related to the coating properties were also estimated using a graphical method, as summarized in Table 4. For the AA-PMMA sample, the CPE behavior associated with the coating (at HF) was only observed after being exposed for one day, revealing an α value around 0.88 and a Q coefficient close to 1.85×10^{-5} ($F\ s^{(\alpha-1)} \cdot cm^{-2}$). For the AA-PBMA sample, the CPE behavior presented an α average of 0.97, thus being larger than AA-PMMA and AA-PHMA, since the frequency distribution was probably lower. The Q coefficient varied from 0.77×10^{-9} to 1.06×10^{-9} $F\ s^{(\alpha-1)}$ over time, this slight increase with time indicated a porosity rise and/or a water up-take through the coating [9,13,15]. For AA-PHMA, CPE behavior was seen in MF and HF, possibly indicating a degradation, as was previously described by Amand et al. [17]. These values were similar than those estimated by fitting, validating the equivalent circuit.

Figure 6 presents the evolution of $|Z|_{LF}$ as a function of the exposure time, and it can be seen that all the samples show a decrease of $|Z|_{LF}$ over time. However, for the sample coated with the AA-PBMA polymer, the decrease occurs more slowly, reaching a plateau after 30 days. This could be attributed to the speed at which the water absorption occurs in the coatings, that is, the speed at which the metal surface is accessed, and the decrease in total impedance due to the contribution of two signals, the coating, and the metal, limiting its protective properties.

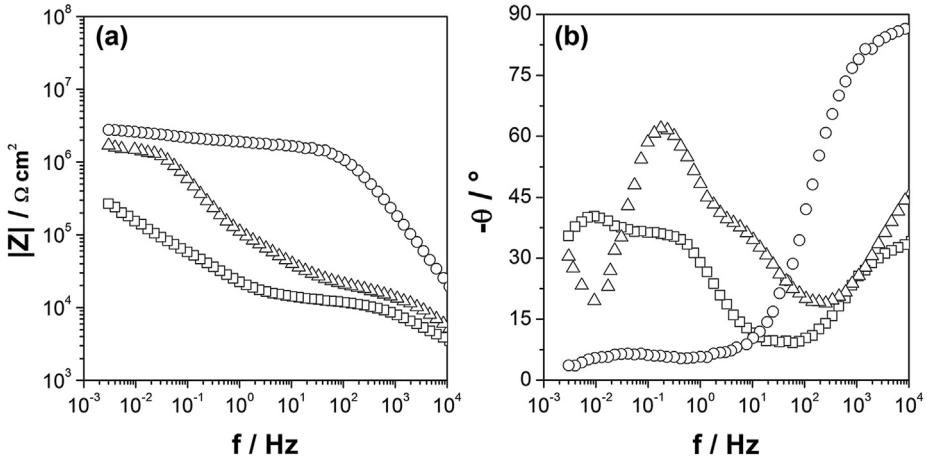

Fig. 5 – Bode plots of coated AA-2024 with (□) AA-PMMA (○) AA-PBMA, and (Δ) AA-PHMA after 56 days being exposure in 0.1 M Na_2SO_4 solution at E = OCP. (a) Modulus and (b) phase.

Table 4 – Impedance parameters of coated samples after exposure.

ID	t/days	$-\alpha_{HF}$	$Q_{eff,HF} \times 10^{-9}$ ($F \cdot s^{(\alpha-1)} \cdot cm^{-2}$)
AA-PMMA	1	0.88	1.8
AA-PBMA	1	0.98	0.7
	7	0.97	0.9
	28	0.97	0.9
	56	0.96	1.1
AA-PHMA	1	0.84	1.6
	7	0.76	14.2

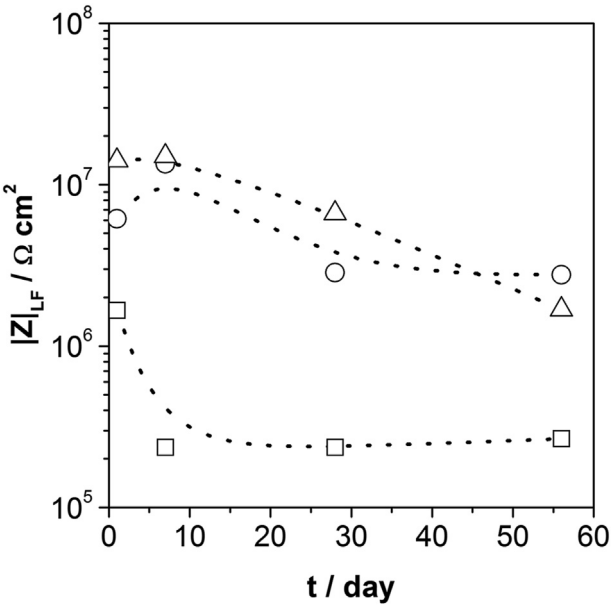

Fig. 6 – Modulus of impedance at low-frequency of (□) AA-PMMA (○) AA-PBMA, and (Δ) AA-PHMA as a function of exposure time.

The infinite capacitances (C_∞) were estimated from the Cole–Cole plot [36], as shown in Fig. 7 for coated samples after 1 and 56 days of immersion. The segmented lines represent the criteria utilized on the C_∞ determination, being by extrapolation to the real capacitance (C_{real}), but where in one case employing the slope of the complex capacitance at HF, and the other case using the complex capacitance value at the highest frequency. The AA-PBMA showed the lowest variation between both criteria. Nevertheless, AA-PBMA and AA-PHMA demonstrated that C_∞ was drastically influenced by the

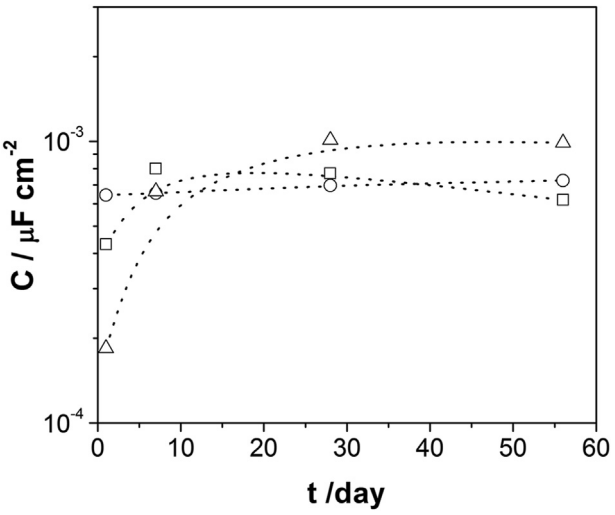

Fig. 8 – Variation of the infinite capacitance of coated AA-2024 as a function of exposure to 0.1 M $NaSO_4$ solution (□) AA-PMMA (○) AA-PBMA, and (Δ) AA-PHMA.

criterium used. Therefore, choosing wrongly can imply a misinterpretation later on.

Furthermore, Fig. 8 shows the variation of the C_∞ obtained from the extrapolation line with a slope for all evaluated systems, revealing that the highest C_∞ value was exhibited by AA-PMMA and AA-PHMA samples, while AA-PBMA remained almost constant across the exposure time.

From C_∞ the coating thickness was estimated as was previously described by Benoit [35], Barrès [42], Tran [43], and A. S. Nguyen [13].

$$C_\infty = \frac{\varepsilon \varepsilon_0}{\delta} \quad (2)$$

where ε_0 and ε are the permittivity of the vacuum and the dielectric constant for the coating [13,18] and equal to 3.3, according to Nguyen et al. [13]. However, the ε of a water-absorbent coating should change when this occurs; in fact, the authors studied organic coatings deposited on AA-2024 by EIS, showing that dielectric constants increased by up to 125% after 42 days, as a result of water absorption in the coatings. Figure 9 shows a comparison of coating thickness for all coatings evaluated assuming a constant ε during the exposure time and a variable ε, as observed by Nguyen et al. [13] and the estimation made by contrasting the thickness values with FE-

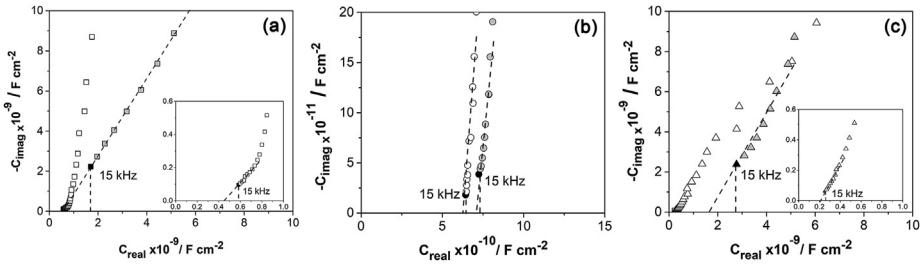

Fig. 7 – Cole–Cole plots of coated AA-2024 with (a) AA-PMMA, (b) AA-PBMA and (c) AA-PHMA samples after being exposure in 0.1 M Na_2SO_4 solution at E = OCP (□,○,Δ) 1 day and (■,●,▲) 56 days.

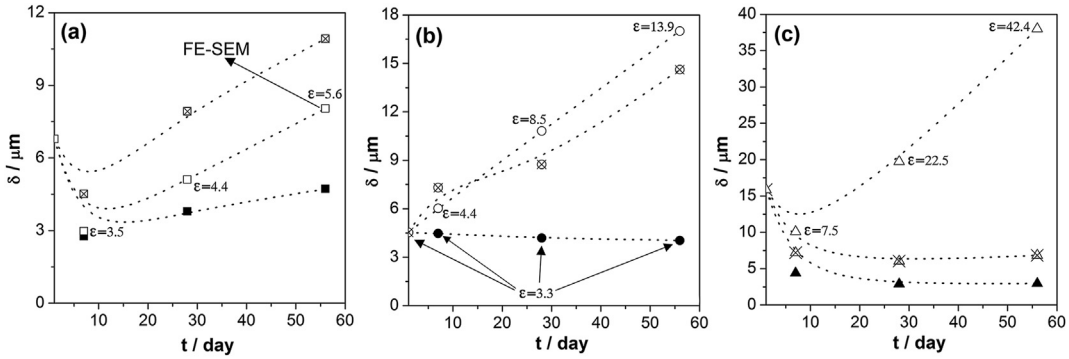

Fig. 9 – Coating thickness comparison with dielectric constant variation across exposure time. (a) PMMA, (b) PBMA and (c) PHMA where (■,■,▲) considering ϵ constant (⊠,⊗,⩙) considering that ϵ increase a 125% until 42 days, and (□,○,Δ) adjusting ϵ according to coating thickness observed by FE-SEM.

SEM images. It should be noted that if ε is invariant throughout the exposure time, the thickness of the coating experiences a slight decrease. Whereas, if ε is estimated as a function of the exposure time, the coating thickness values are possibly closer to the real values. FE-SEM images reveal that all coatings evaluated are thicker after 56 days, averaging 8.33 μm, 16.79 μm, and 38.73 μm for AA-PMMA, AA-PBMA, and AA-PHMA, respectively (see Fig. 3 (d–f)). By considering these coating thicknesses, the dielectric constant was estimated after 56 days of exposure for each sample, as shown in Fig. 9 (in open symbols). Therefore,

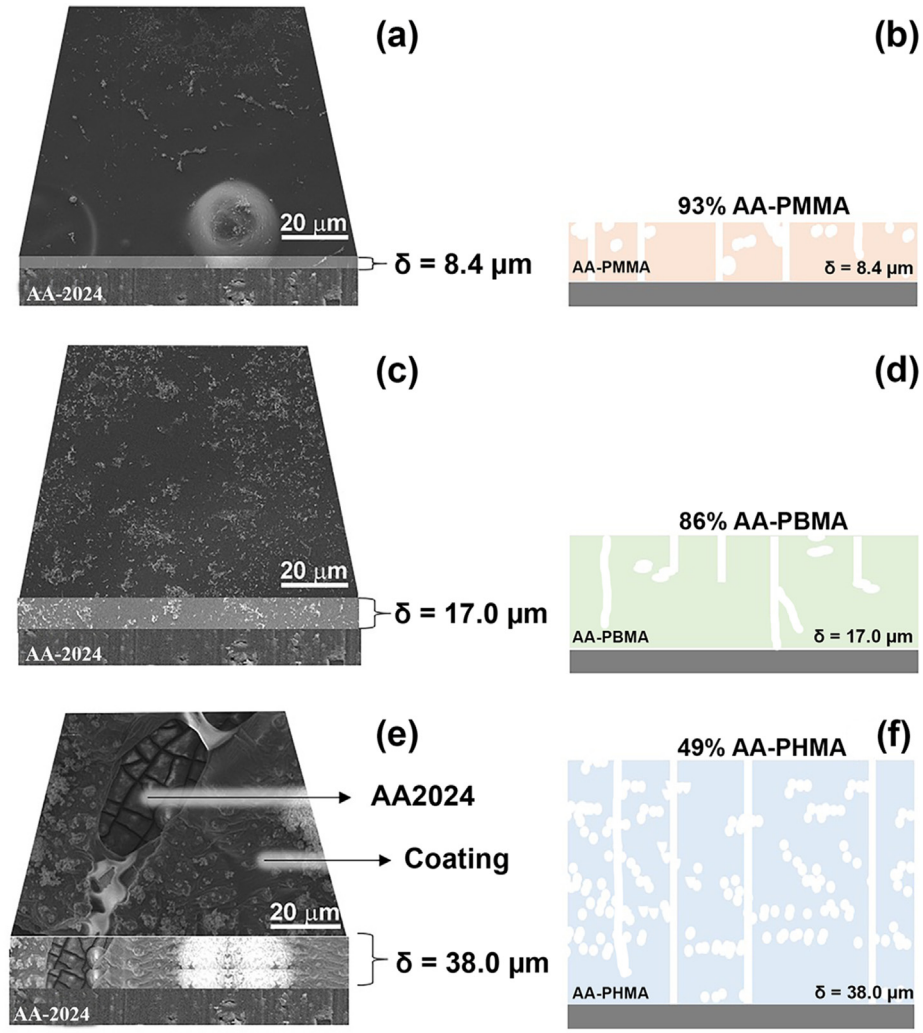

Fig. 10 – SEM images and schematic representation of coatings after 56 days of exposure in 0.1 M Na_2SO_4 solution (a,b) AA-PMMA (c,d) AA-PBMA and (e,f) AA-PHMA.

experimental evidence suggests that the coating thickens over exposure time due to water uptake, which implies an increase in the dielectric constant under immersion.

Figure 10 shows the SEM images of coated samples after 56 days of exposure (top view) and a schematic representatión of the same sample. The increase in thickness was according to the alkyl side chain for longer exposure times; this means that the AA-PHMA proved to be thicker after 56 days than the AA-PMMA. However, from an electrochemical point of view, AA-PBMA showed the best performance when compared to the other polymers, with a lower presence of the metal response, which is in agreement with the images. As can be seen, the AA-PBMA showed a more homogeneous surface even after 56 days of exposure. The dielectric constant (ε) of the polymer increased over time as water entered, thus once the dielectric constant was estimated, the contribution of each to the constant was achieved.

4. Conclusions

The thickness of the different polymethyl methacrylates prepared by photopolymerization on AA2024 surfaces, previously treated with a plasma-Argon-based protocol, presented thicknesses between 1 and 6 μm, as estimated by GD-OES and FE-SEM measurements. These differences seem to be associated with the morphological differences of the polymethyl methacrylates and the existence of a critical chain length to achieve adequate and desirable degrees of compaction and hydrophobicity in anticorrosive coatings.

AFM images reveal that an increase in the length of the alkyl chain promotes an increase in the population density of defects in the coatings and the surface hydrophobic properties. However, FE-SEM analyzes contradict the apparent increase in surface hydrophobicity with chain length. These images reveal in all cases a coating thickness increase, which was associated with water permeability. However, the thickness changes associated with water absorption were less marked for the AA-PBMA sample. On the other hand, electrochemical responses revealed that the protective efficiency of the coatings was not proportionally related to the side chain length, as was originally proposed. AA-PBMA (four-carbon alkyl chain) was the least deteriorated and with the best protective characteristics. Even so, this polymer had a water absorption of around 14% after 56 days of exposure to the electrolyte.

Declaration of Competing Interest

The authors declare that they have no known competing financial interests or personal relationships that could have appeared to influence the work reported in this paper.

Acknowledgments

The authors would like to thank POSTDOC Dicyt (Code 029142 PC_POSTDOC), CONICYT-Fondecyt (Grants 1180843 and 1160604), CONICYT-Fondequip (Grant EQM 160091 and EQM 15010) for financial support.

Appendix A. Supplementary data

Supplementary data to this article can be found online at https://doi.org/10.1016/j.jmrt.2021.11.067.

REFERENCES

[1] Dalmoro V, Dos Santos JHZ, Armelin E, Alemán C, Azambuja DS. A synergistic combination of tetraethylorthosilicate and multiphosphonic acid offers excellent corrosion protection to AA1100 aluminum alloy. Appl Surf Sci 2013;273:758–68. https://doi.org/10.1016/j.apsusc.2013.02.131.

[2] Ahuir-Torres JI, Arenas MA, Perrie W, Dearden G, de Damborenea J. Surface texturing of aluminium alloy AA2024-T3 by picosecond laser: effect on wettability and corrosion properties. Surf Coating Technol 2017;321:279–91. https://doi.org/10.1016/j.surfcoat.2017.04.056.

[3] Blanc C, Pébère N, Tribollet B, Vivier V. Galvanic coupling between copper and aluminium in a thin-layer cell. Corrosion Sci 2010;52:991–5. https://doi.org/10.1016/j.corsci.2009.11.023.

[4] Surca AK, Rauter A, Rodošek M, Slemenik Perše L, Koželj M, Orel B. Modified bis-(3-(3-(3-triethoxysilyl)propyl)thioureido) propyl terminated poly(dimethylsiloxane)/POSS protective coatings on AA 2024. Prog Org Coating 2017;103:1–14. https://doi.org/10.1016/j.porgcoat.2016.11.023.

[5] Rodič P, Milošev I, Lekka M, Andreatta F, Fedrizzi L. Study of the synergistic effect of cerium acetate and sodium sulphate on the corrosion inhibition of AA2024-T3. Electrochim Acta 2019;308:337–49. https://doi.org/10.1016/j.electacta.2019.04.042.

[6] Thirumoolan D, Siva T, Sathiyanarayanan S, Anver Basha K, Kaviyarasu K, Ayeshamariam A, et al. Study on anticorrosion behavior of poly(N-vinylimidazole-co-methoxyethyl methacrylate) based coating in the aggressive chloride ion environment. J Adv Microsc Res 2018;13:20–32. https://doi.org/10.1166/jamr.2018.1353.

[7] Laco JII, Villota FC, Mestres FL. Corrosion protection of carbon steel with thermoplastic coatings and alkyd resins containing polyaniline as conductive polymer. Prog Org Coating 2005;52:151–60. https://doi.org/10.1016/j.porgcoat.2004.10.005.

[8] Muñoz L, Tamayo L, Gulppi M, Rabagliati F, Flores M, Urzúa M, et al. Surface functionalization of an aluminum alloy to generate an antibiofilm coating based on poly(methyl methacrylate) and silver nanoparticles. Molecules 2018;23. https://doi.org/10.3390/molecules23112747.

[9] Perrin FX, Nguyen VN, Vernet JL. Water absorption characteristics of hybrid materials incorporating tetrabutyl titanate with acrylic polymer via sol-gel process. J Appl Polym Sci 2005;97:92–102. https://doi.org/10.1002/app.21736.

[10] Funke W. Thin-layer technology in organic coatings. Prog Org Coating 1996;28:3–7. https://doi.org/10.1016/0300-9440(95)00583-8.

[11] Ranjithkumar B, Safiullah SM, Babu K, Basha KA. Synthesis and characterization of methacrylate-based antibacterial copolymers for anticorrosive application. Polym - Plast Technol Eng 2018;57:657–68. https://doi.org/10.1080/03602559.2017.1344850.

[12] Nazeer AA, Al-Hetlani E, Amin MO, Quiñones-Ruiz T, Lednev IK. A poly(butyl methacrylate)/graphene oxide/TiO2 nanocomposite coating with superior corrosion protection for AZ31 alloy in chloride solution. Chem Eng J 2019;361:485–98. https://doi.org/10.1016/j.cej.2018.12.077.
[13] Nguyen AS, Causse N, Musiani M, Orazem ME, Pébère N, Tribollet B, et al. Determination of water uptake in organic coatings deposited on 2024 aluminium alloy: comparison between impedance measurements and gravimetry. Prog Org Coating 2017;112:93–100. https://doi.org/10.1016/j.porgcoat.2017.07.004.
[14] Bellucci F, Nicodemo L. Water transport in organic coatings8; 1993. p. 49.
[15] Miszczyk A, Darowicki K. Water uptake in protective organic coatings and its reflection in measured coating impedance. Prog Org Coating 2018;124:296–302. https://doi.org/10.1016/j.porgcoat.2018.03.002.
[16] Castela AS, Sim AM. An impedance model for the estimation of water absorption in organic coatings . Part I : a linear dielectric mixture equation. Corrosion Sci 2003;45:1631–46. https://doi.org/10.1016/S0010-938X(03)00014-3.
[17] Amand S, Musiani M, Orazem ME, Pébère N, Tribollet B, Vivier V. Constant-phase-element behavior caused by inhomogeneous water uptake in anti-corrosion coatings. Electrochim Acta 2013;87:693–700. https://doi.org/10.1016/j.electacta.2012.09.061.
[18] Nguyena AS, Musianib M, Orazemc ME, Pébèrea N, Tribolletd B, Vivier V. Impedance study of the influence of chromates on the properties of waterborne coatings deposited on 2024 aluminium alloy. Corrosion Sci 2016;109:174–81. https://doi.org/10.1016/j.corsci.2016.03.030.
[19] Pletincx S, Fockaert LLI, Mol JMC, Hauffman T, Terryn H. Probing the formation and degradation of chemical interactions from model molecule/metal oxide to buried polymer/metal oxide interfaces. Npj Mater. Degrad. 2019;3:1–12. https://doi.org/10.1038/s41529-019-0085-2.
[20] Muñoz L, Pineda F, Martínez C, Sancy M, Urzua M, Flores M, et al. Surface & Coatings Technology Improving the interaction between aluminum surfaces and polymer coatings. Surf Coating Technol 2019;358:435–42. https://doi.org/10.1016/j.surfcoat.2018.11.051.
[21] Guerra C, Ringuedé A, Azocar MI, Walter M, Galarce C, Bedioui F, et al. Corrosion analysis of AISI 430 stainless steel in the presence of Escherichia coli and Staphylococcus aureus. Corrosion Sci 2021;181. https://doi.org/10.1016/j.corsci.2020.109204.
[22] Heine MA, Keir DS, Pryor MJ. The specific effects of chloride and sulfate ions on oxide covered aluminum. J Electrochem Soc 1965;112:24. https://doi.org/10.1149/1.2423459.
[23] Parangusan H, Bhadra J, Al-Thani N. A review of passivity breakdown on metal surfaces: influence of chloride- and sulfide-ion concentrations, temperature, and pH. Emergent Mater 2021. https://doi.org/10.1007/s42247-021-00194-6.
[24] Murakami D, Jinnai H, Takahara A. Wetting transition from the cassie-baxter state to the wenzel state on textured polymer surfaces. Langmuir 2014;30:2061–7. https://doi.org/10.1021/la4049067.
[25] Mchale G. Cassie and wenzel : were they really so wrong ?43; 2007. p. 8200–5.
[26] Milne AJBB, Amirfazli A, Baxter C. The Cassie equation : how it is meant to be used. Adv Colloid Interface Sci 2012;170:48–55. https://doi.org/10.1016/j.cis.2011.12.001.
[27] Bobji MS, Kumar SV, Asthana A, Govardhan RN. Underwater sustainability of the "Cassie" state of wetting. Langmuir 2009;25:12120–6. https://doi.org/10.1021/la902679c.
[28] Briones XG, V Encinas M, Petri DFS, Pavez JE, Tapia RA, Urz MD. Adsorption behavior of hydrophobically modified polyelectrolytes onto amino- or methyl-terminated surfaces. Langmuir 2011:13524–32.
[29] Islam MS, Tong L, Falzon PJ. Influence of metal surface preparation on its surface profile, contact angle, surface energy and adhesion with glass fibre prepreg. Int J Adhesion Adhes 2014;51:32–41. https://doi.org/10.1016/j.ijadhadh.2014.02.006.
[30] Kosaka PM, Kawano Y, Petri DFS. Dewetting and surface properties of ultrathin films of cellulose esters. J colloid interface sci 2007;316:671–7. https://doi.org/10.1016/j.jcis.2007.07.058.
[31] Lobo L, Fernández B, Pereiro R. Depth profile analysis with glow discharge spectrometry. J. Anal. At. Spectrom. 2017;32:920–30. https://doi.org/10.1039/c7ja00055c.
[32] Marin E, Guzman L, Lanzutti A, Ensinger W, Fedrizzi L. Multilayer Al 2O 3/TiO 2 atomic layer deposition coatings for the corrosion protection of stainless steel. Thin Solid Films 2012;522:283–8. https://doi.org/10.1016/j.tsf.2012.08.023.
[33] Zhao J, Lu P, Song L, Tian L, Ming W, Ren L. Highly efficient antifogging and frost-resisting acrylic coatings from one-step thermal curing. Colloids Surfaces A Physicochem. Eng. Asp. 2020;585:124160. https://doi.org/10.1016/j.colsurfa.2019.124160.
[34] Sancy M, Gourbeyre Y, Sutter EMM, Tribollet B. Mechanism of corrosion of cast iron covered by aged corrosion products : application of electrochemical impedance spectrometry. Corrosion Sci 2010;52:1222–7. https://doi.org/10.1016/j.corsci.2009.12.026.
[35] Benoit M, Bataillon C, Gwinner B, Miserque F, Orazem ME, Sánchez-Sánchez CM, et al. Comparison of different methods for measuring the passive film thickness on metals. Electrochim Acta 2016;201:340–7. https://doi.org/10.1016/j.electacta.2015.12.173.
[36] Truc TA, Thuy TT, Oanh VK, Hang TTX, Nguyen AS, Caussé N, et al. 8-Hydroxyquinoline-Modified clay incorporated in an epoxy coating for the corrosion protection of carbon steel. Surfaces and Interfaces 2019;14:26–33. https://doi.org/10.1016/j.surfin.2018.10.007.
[37] Boucher D, Ladmiral V, Negrell C, Caussé N, Pébère N. Partially acrylated linseed oil UV-cured coating containing a dihemiacetal ester for the corrosion protection of an aluminium alloy. Prog Org Coating 2021;158. https://doi.org/10.1016/j.porgcoat.2021.106344.
[38] Orazem ME, Tribollet B. Electrochemical impedance spectroscopy. Hoboken, NJ, USA: John Wiley & Sons; 2017. https://doi.org/10.1002/9781119363682.
[39] Harb SV, Trentin A, Uvida MC, Magnani M, Pulcinelli SH, Santilli CV, et al. A comparative study on PMMA-TiO2 and PMMA-ZrO2 protective coatings. Prog Org Coating 2020;140. https://doi.org/10.1016/j.porgcoat.2019.105477.
[40] Harb SV, Trentin A, de Souza TAC, Magnani M, Pulcinelli SH, Santilli CV, et al. Effective corrosion protection by eco-friendly self-healing PMMA-cerium oxide coatings. Chem Eng J 2020;383:123219. https://doi.org/10.1016/j.cej.2019.123219.
[41] Coquery C, Carosio F, Negrell C, Caussé N, Pébère N, David G. New bio-based phosphorylated chitosan/alginate protective coatings on aluminum alloy obtained by the LbL technique. Surfaces and Interfaces 2019;16:59–66. https://doi.org/10.1016/j.surfin.2019.04.010.
[42] Barrès T, Tribollet B, Stephan O, Montigaud H, Boinet M, Cohin Y. Characterization of the porosity of silicon nitride thin layers by Electrochemical Impedance Spectroscopy. Electrochim Acta 2017;227:1–6. https://doi.org/10.1016/J.ELECTACTA.2017.01.008.
[43] Tran TTM, Tribollet B, Sutter EMM. New insights into the cathodic dissolution of aluminium using electrochemical methods. Electrochim Acta 2016;216:58–67. https://doi.org/10.1016/J.ELECTACTA.2016.09.011.